This article has been accepted for publication in a future issue of this journal, but has not been fully edited. Content may change prior to final publication. Citation information: DOI 10.1109/JSTARS.2020.2984568, IEEE Journal of Selected Topics in Applied Earth Observations and Remote Sensing

Spectral-spatial classification integrating band selection for hyperspectral imagery with severe noise bands

Ji Zhao, Suzheng Tian, Christian Geiß, Lizhe Wang, Yanfei Zhong, Hannes Taubenböck

***Abstract*—Spectral-spatial classification for hyperspectral imagery has been receiving much attention, since the detailed spectral and rich spatial information of hyperspectral images can be fully exploited to improve the classification accuracy. However, when the original hyperspectral images have very noisy bands, these bands may have an unfavorable impact on the classification, and are often discarded in advance based on expert knowledge. In this study, a spectral-spatial conditional random field classification algorithm integrating band selection (CRFBS) is developed for hyperspectral imagery with severe noise bands. The proposed algorithm integrates band selection based on the relative utility of the spectral bands for classification. Consequently, negative effects of severe noise bands are eliminated and the need for high-quality image data is substantially reduced. In addition, the CRFBS algorithm makes comprehensive use of both the spectral and the spatial cues to improve the classification performance. The spectral cues are formulated by integrating the support vector machine and random forest algorithms to improve the spectral discriminative ability in the unary potentials, and the spatial information are modeled to consider the interactions between pixels in pairwise potentials. The experiments using different airborne and UAV-borne hyperspectral data verified the effectiveness of the CRFBS method. The CRFBS algorithm can achieve accurate interpretation of the various classification categories and a more than 3% improvement in classification accuracy, compared with the method using the original hyperspectral image with severe noise bands.**

***Index Terms*—Conditional random fields, Hyperspectral image, Image classification, Random forest, Spectral-spatial classification**

Manuscript received January 22, 2020; revised March 6, 2020; accepted March 17, 2020. This work was supported by National Natural Science Foundation of China under Grant Nos. 41801280, U1711266, 41925007, and 41771385, Fundamental Research Funds for the Central Universities, China University of Geosciences (Wuhan) under Grant CUG170676. (*Corresponding author: Lizhe Wang*)

J. Zhao is with the School of Computer Science, China University of Geosciences, Wuhan 430074, China, and also with the German Aerospace Center (DLR), German Remote Sensing Data Center (DFD), Oberpfaffenhofen 82234, Germany (e-mail: zhaoji@cug.edu.cn).

S. Tian and L. Wang are with the School of Computer Science, China University of Geosciences, Wuhan 430074, China (e-mail: tiansuzheng@cug.edu.cn; lizhe.wang@gmail.com).

C. Geiß and H. Taubenböck are with the German Aerospace Center (DLR), German Remote Sensing Data Center (DFD), Oberpfaffenhofen 82234, Germany (e-mail: Christian.Geiss@dlr.de; Hannes.Taubenboeck@dlr.de).

Y. Zhong is with the State Key Laboratory of Information Engineering in Surveying, Mapping and Remote Sensing, Wuhan University, Wuhan 430079, China (e-mail: zhongyanfei@whu.edu.cn).

I. INTRODUCTION

HYPERSPECTRAL imagery is a very important data source for deriving detailed thematic information on the earth surface, since it contains hundreds of narrow spectral channels to distinguish the subtle spectral difference of various materials [1, 2]. Therefore, hyperspectral image classification is an enduring research topic [3]. Hyperspectral image classification aims at labeling each pixel with specific semantic categories, and can be used for manifold applications [4], such as precision agriculture, mineral mapping, or environmental monitoring. However, in the classification process there is a strong correlation between hundreds of narrow spectral bands, which results in redundant information content and high spectral dimensionality. This can lead to a high-dimensional processing problem, the so-called Hughes phenomenon [5], if only a limited number of training samples are available.

To solve high-dimensional problems in hyperspectral image classification when the samples cannot be significantly increased, there are two options: first, to reduce the dimension of the hyperspectral data, and second, to improve the processing capability of classifiers that use high dimensional features. Dimensionality reduction can be achieved by band selection or feature extraction to solely retain useful information [6]. Feature extraction creates new features in a feature space with lower dimensionality while satisfying certain criteria regarding the original spectral features [7, 8]. Such techniques comprise linear discriminant analysis and principal component analysis, among others. In contrast, band selection is to select representative band subsets from the original spectral channels to preserve important information and reduce the number of bands [9, 10]. Examples are the band selection method based on saliency bands and scale selection (SBSS) [11] and the salient band selection method based on manifold ranking [12].

For classification, there are methods that have the ability to deal with the problem of learning a robust model from a high-dimensional feature vector in conjunction with limited training samples. Support Vector Machine (SVM) and Random Forest (RF) are typical classification algorithms, which have received extensive attention in hyperspectral classification [13, 14]. SVM is a discriminative classifier to find a decision boundary that effectively separates different classes. The decision boundary is a separating hyperplane formed by support vectors, and can distinguish complex two-class scenes based on the kernel technique [15]. Among numerous supervised pixel-wise image classification algorithms (such as neural network and RF methods), SVM is considered to achieve the highest accuracy [16]. However, RF is a typical ensemble learning algorithm to combine multiple decision tree classifiers to achieve a stable and better classification performance compared to individual models. RF randomly selects spectral feature subsets, and is insensitive to data with some missing features as well as noisy features. More importantly, RF can not only handle classification problems with high-dimensional feature spaces like SVM, but it also allows for interpretability by enabling to estimate which variables play an important role in the classification. Therefore, RF is widely used in image classification [13], and has a series of extended models, such as rotation forest [17, 18], among others. These pixel-wise classification algorithms process each pixel independently based on spectral information without considering spatial correlation between pixels, and always have obvious salt-and-pepper classification results which affect classification accuracy negatively.

To improve classification performance, spatial information of hyperspectral imagery can be additionally exploited. The spectral-spatial classification approaches comprehensively utilize spectral and spatial information to help accurately recognize semantic categories [19], and lots of spectral-spatial classification algorithms have been developed [3, 20, 21]. Object-oriented and deep learning approaches have often been applied. For the object-oriented classification, it takes objects as the processing unit [22-25] to consider the spatial information. The objects are first generated by segmentation, such as the fractal net evolution approach (FNEA) [26]. The object features obtained from spatial statistics of pixels in an object can be used to enable final classification results. A majority voting strategy within each object is another way to obtain the labels using pixel-wise classification [27]. For spectral-spatial methods based on deep learning, the approach can mine the spatial structure information of the images by a designed network structure [28-30]. For example, as an effective deep learning model, convolutional neural network (CNN) is mainly composed of a series of convolution and pooling layers to extract effective spatial structure features, and uses a stack of fully connected layers to perform the classification tasks [31]. Combining the characteristics of hyperspectral remote sensing images, CNN has developed a number of models for hyperspectral classification task [30], such as the spectral-spatial attention network with an attention mechanism [32] and spectral-spatial residual network using 3-D convolutional layer [33]. These CNN classification frameworks can achieve good classification performance. However, these classification models based on deep learning often require a large number of training sets to optimize a mass of parameters in the network structure.

Beyond that, the random field model is another method to explicitly model spatial information by constructing the correspondence between images and graphs. The Markov random field and conditional random field (CRF) models are widely used random field models in image processing [34-36]. For hyperspectral image classification, multiple research works about random fields have been carried out to deal with specific issues. For example, a spectral-spatial classification method using CRF and active learning was proposed to use spatial and spectral information to enlarge the training set efficiently [37]. The rotation forests with local feature extraction was used to model the potential functions of MRF to improve classification accuracy [17]. A spectral-spatial classification method inspired by game theory was developed to use a cooperative game to obtain final classification results [38]. These classification algorithms achieve good classification performance by considering the spatial information, compared to pixel-wise classification algorithms. However, they often depend on the ability of potential functions to model the relationship between classification labels and the hyperspectral image, and are sensitive to the quality of hyperspectral data. The input original hyperspectral image often have very noisy bands, and may even have bands which carry solely zero values and do not contain any useful information. These noise bands, such as water absorption bands, have a certain impact on classification, and are often removed in advance based on expert knowledge.

In order to mitigate the effect of noise bands and to improve the robustness of the random field model for hyperspectral data, we develop a spectral-spatial conditional random field classification algorithm integrating band selection (CRFBS) for hyperspectral imagery with severe noise bands. In the CRFBS algorithm, the potential functions are used to model the posterior probability to achieve the classification labels, which depend on the quality of hyperspectral data. Accordingly, the band selection based on the relative utility of the spectral bands is proposed to provide ideal data. The traditional band selection method selects information metrics independent of classification tasks, such as information gain, which may not be able to improve classification performance. In contrast, the proposed band selection method selects the relative importance of the spectral bands as an effective measure to select important bands, which is directly related to the classification task and can be used to distinguish the various classes. To alleviate the uncertainty between spectrum and category mapping, the selected bands with greater impact on classification and spatial contextual information are exploited by potential functions of CRF model to improve the classification performance. The unary potential is formulated by the class membership probabilities to provide the basic discriminative information of various semantic classes based on the spectral cues, and the pairwise potential models the spatial interactions between image pixels to favor the homogenous regions of a hyperspectral image take the same classification label in the classification map. In summary, the main contributions of this work are as follows: (1) the band selection based on the relative utility of the spectral bands is developed to select the important bands. (2) The band selection is integrated in the CRFBS algorithm to automatically alleviate the effects of severe noise bands. (3) Both the spectral and the spatial cues are exploited based on potential functions of the CRF model to improve classification performance.

This article has been accepted for publication in a future issue of this journal, but has not been fully edited. Content may change prior to final publication. Citation information: DOI 10.1109/JSTARS.2020.2984568, IEEE Journal of Selected Topics in Applied Earth Observations and Remote Sensing

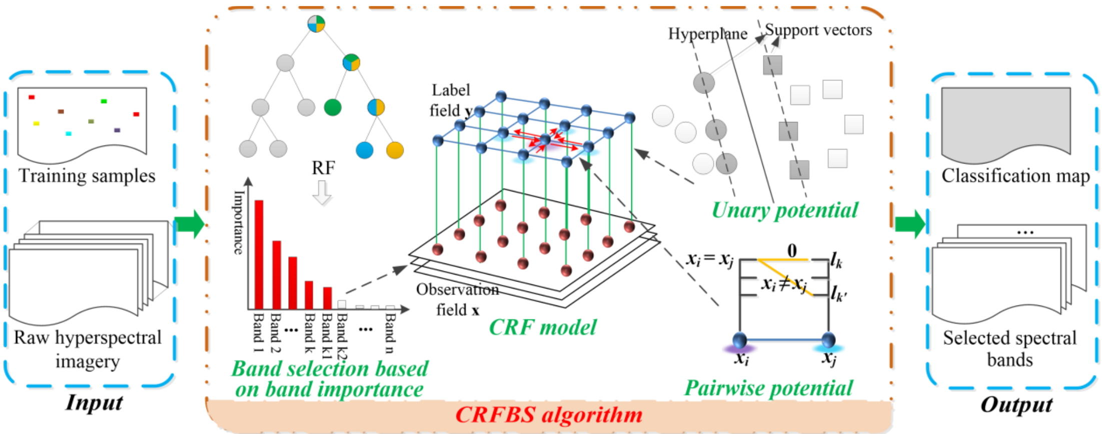

Fig. 1. The framework of the spectral-spatial conditional random field classification integrating band selection (CRFBS).

The effectiveness of the CRFBS algorithm was tested using different hyperspectral datasets with some bands contaminated with severe noise, and the experimental results showed that the CRFBS method has a competitive classification performance, compared with other state-of-the-art hyperspectral image classification approaches.

In the rest of this paper, we describe the proposed CRFBS algorithm in Section II, present the used experimental data (Section III), show the corresponding experimental results in Section IV, give several necessary analysis for the proposed algorithm (Section V) and draw conclusions in Section VI.

II. The Proposed CRFBS Method

To eliminate the effects of severe noise bands, the CRFBS algorithm is proposed in this section. As shown in Fig. 1, the CRFBS approach contains four main interlinked modules: (1) the core CRF model is constructed to provide spectral-spatial classification framework. (2) The band selection based on band importance measure selects the spectral bands useful for classification by sorting the importance of each band to obtain ideal observation data for CRF model. (3) The unary potential models the relationship between classification labels and observation data by the class membership probabilities, which is obtained by non-linear SVM. (4) The pairwise potential models the spatial interactions of neighboring pixels to encode the spatial patterns of classification classes. These modules are detailed in the following four subsections.

A. *The CRF framework*

The classification of hyperspectral images aims to find the optimal pixel label using known spectral cues of the image, and can be considered as maximizing *a posteriori* probability of the category labels using the input hyperspectral image. As a widely used probabilistic graphical model, CRF attempts to directly model *a posteriori* probability to consider the spatial information using the correspondence between images and graphs [36]. Consider an original input hyperspectral image $\mathbf{x}=\{\mathbf{x}_1, \mathbf{x}_2,\ldots, \mathbf{x}_N\}$, where $\mathbf{x}_i$ represents the spectral values of image pixel $i \in V = \{1, 2, \cdots, N\}$, and N is the number of pixels. The classification label can be denoted as $\mathbf{y}=\{y_1, y_2,\ldots,y_N\}$, where each label y_i of image pixel i takes a value from the label set $L=\{1,2,\ldots,K\}$, and K is the number of classes. Thereby, CRF can use a Gibbs distribution to model *a posteriori* probability [39]:

$$P(\mathbf{y} \mid \mathbf{x}) = \frac{1}{Z}\exp\left\{-\sum_{c\in C}\psi_c(\mathbf{y}_c, \mathbf{x})\right\} \tag{1}$$

where Z represents the partition function. $\psi_c(\mathbf{y}_c, \mathbf{x})$ is called the potential function and is a positive function of random variables in the clique c, which can be divided into unary, pairwise, and even higher-order potential functions according to the different types of cliques. Considering the inference difficulty for a general higher-order potential function, the CRF including unary and pairwise potential functions is widely used:

$$P(\mathbf{y} \mid \mathbf{x}) = \frac{1}{Z}\exp\left\{-\sum_{i\in V}\psi_i(y_i \mid \mathbf{x}) - \lambda \sum_{i\in V, j\in N_i}\psi_{ij}(y_i, y_j \mid \mathbf{x})\right\} \tag{2}$$

where $\psi_i(y_i \mid \mathbf{x})$ and $\psi_{ij}(y_i, y_j \mid \mathbf{x})$ represent the unary potential term and pairwise potential term to model the dependencies of pairs of random variables, respectively. N_i is the local neighborhood of pixel i, and 8-neighborhood connectivity is widely used to encode the spatial-contextual relationship [40]. λ controls the strength of the pairwise potential term relative to the unary potential term. The posteriori probability based on Eq.(2) is converted to the corresponding Gibbs energy:

$$\begin{aligned} E(\mathbf{y} \mid \mathbf{x}) &= -\log(P(\mathbf{y} \mid \mathbf{x})) - \log(Z) \\ &= \sum_{i\in V}\psi_i(y_i \mid \mathbf{x}) + \lambda \sum_{i\in V, j\in N_i}\psi_{ij}(y_i, y_j \mid \mathbf{x}) \end{aligned} \tag{3}$$

It can be seen that the classification problem can minimize equivalently the energy function $E(\mathbf{y}|\mathbf{x})$ to obtain the optimal classification label $\mathbf{y}$. To minimize the energy function, we apply the graph-cut inference algorithm [41] in our study, as it is considered an efficient approximation method.

The general CRF framework is established for hyperspectral image classification, and the remaining problem is to formulate unary and pairwise potential terms. Based on Eq.(3), the unary and pairwise potential functions can be considered to depend on the input hyperspectral image $\mathbf{x}$. Accordingly, the noisy bands in the input original hyperspectral image will affect the

This article has been accepted for publication in a future issue of this journal, but has not been fully edited. Content may change prior to final publication. Citation information: DOI 10.1109/JSTARS.2020.2984568, IEEE Journal of Selected Topics in Applied Earth Observations and Remote Sensing

effective construction of these potential functions and have a further impact on the spectral-spatial classification performance. To eliminate the effects of the noisy bands, the band selection based on the relative importance is integrated in the CRF framework and is also introduced in the following subsection.

B. Band selection based on band importance measure

Hyperspectral images often have many spectral bands, which have different discriminative capabilities for distinguishing classification categories because they are in the different parts of the spectrum [42]. Some bands that are more useful for distinguishing categories have greater importance. Some bands contain severe noise and even have no information value, so they have no positive effect on classification. In this study we develop band selection based on band importance measure to eliminate the effects of severe noise bands and select useful bands for classification. The importance of the bands is first obtained, and then the spectral bands with high importance are selected based on the given cumulative band importance keeping ratio.

To measure band importance, we apply the RF classification method, which is a widely used ensemble algorithm. The RF algorithm was proposed to overcome the overfitting problem of decision trees based on the aggregation of multiple decision trees, i.e., bagging [43]. It has an excellent performance in hyperspectral classification [13, 44, 45] due to its high-dimensional data processing capabilities. Another potential feature of RF algorithms is the ability to measure relationships between input features and output variables, which is denoted as variable importance. The variable importance in the RF method can be calculated based on the average value of cumulative reduction in node impurity for all the trees of the ensemble. Accordingly, the importance value of a variable X^m is calculated by averaging the sum of the weighted node impurity reductions of all nodes t using X^m over all N_T trees in the forest for estimating Y.

$$Imp(X^m) = \frac{1}{N_T} \sum_{T} \sum_{t \in T : v(s_t) = X^m} p(t) \Delta i(s_t, t) \tag{4}$$

where $p(t)$ is the weight and can be calculated by the proportion of samples reaching node t. $v(s_t)$ represents the variable used in the split s_t and $\Delta i(s_t, t)$ is the impurity reduction of the split s_t at node t. To select spectral bands that are useful for classification, the spectral bands of hyperspectral images are used as input variables of the RF algorithm. Accordingly, the band importance obtained by Eq. (4) can reveal the different roles of each spectral band in the classification, which can be exploited to select the spectral bands that play an important role in classification. To obtain the final spectral band set, we sort by spectral band importances in descending order, and select the spectral bands by setting a threshold of cumulative band importance keeping ratio.

$$\overline{Ind} = \arg\min_{Ind} \sum_{i=1}^{Ind} SortedImp(X^i) > \sum_{i=1}^{B} SortedImp(X^i) * \delta \tag{5}$$

$$SelBands = \left\{ X^i \mid Imp(X^i) > SortedImp(X^{\overline{Ind}}) \right\} \tag{6}$$

where $SortedImp(X^i)$ represents the sorted band importance in descending order and B is the band number of the original input hyperspectral image. Eq. (5) aims to find the first subscript $\overline{Ind}$ of the sorted band importance to satisfy the cumulative proportion of the sorted band importance is greater than the given threshold σ. We obtain the band importance threshold based on the calculated subscript, so that we can select the spectral bands that the corresponding band importance is greater than the band importance threshold, according to Eq.(6). The top ranked bands have greater importance and play a greater role in classification, so that severe noise bands can be discarded automatically due to their lower importance.

C. Unary Potential

The unary potential function of CRF framework mainly models the relationship between category labels and image features, and calculates the cost of each pixel taking a classification label using the selected spectral bands. In the hyperspectral image classification tasks, the unary potential term is formulated by the class membership probabilities, which can be obtained by discriminative classifier using the selected spectral bands. Accordingly, the used unary potential is formulated as:

$$\psi_i(y_i \mid \mathbf{x}) = -\ln\left(P\left(y_i = l_k \mid \overline{\mathbf{x}}\right)\right), \overline{\mathbf{x}} \subseteq \mathbf{x} \tag{7}$$

The unary potential term of CRF uses the class membership probabilities of pixel $P(y_i = l_k)$ to calculate the cost of taking class label l_k at the hyperspectral image i based on the the selected spectral bands $\overline{\mathbf{x}}$. The class membership probabilities can be obtained by any discriminative classifier. In this study, the SVM with nonlinear Gaussian radial basis function (RBF) kernel is used to obtain the probability because the classification categories are not linearly separable in hyperspectral image classification and the non-linear SVM can achieve excellent classification performance using limited training samples. To obtain the class membership probabilities of SVM, the Platt's formulation is used to give the probability estimates based on the class label outputs of SVM, which is implemented in the LIBSVM library [46]. Since the SVM algorithm is sensitive to severe noise bands, a subset of bands obtained by band selection is used to exclude the interference effects of unimportant bands for hyperspectral image classification. Considering that the selected band is based on band importance measure from RF, the unary potential term can be considered to indirectly combine the advantages of the RF and SVM algorithms in the CRFBS classification framework to more accurately distinguish the different categories for hyperspectral imagery with severe noise bands.

D. Pairwise Potential

The pairwise potential function of CRF framework models the spatial interactions between pixels based on the spatial patterns of classification classes that neighboring pixels in a homogeneous area tend to take the same label. The spatial prior knowledge is of importance to help mitigate the classification uncertainty based on spectral information and alleviate the

This article has been accepted for publication in a future issue of this journal, but has not been fully edited. Content may change prior to final publication. Citation information: DOI 10.1109/JSTARS.2020.2984568, IEEE Journal of Selected Topics in Applied Earth Observations and Remote Sensing

effects of salt-and-pepper classification noise. Accordingly, the used pairwise potential is formulated as the following form to encourage the neighborhood pixels of a hyperspectral image to take the same class label [40].

$$\psi_{ij}\left(y_i, y_j \mid \mathbf{x}\right) = \begin{cases} 0 & if\ y_i = y_j \\ \dfrac{1+\theta\exp(-\|\bar{\mathbf{x}}_i - \bar{\mathbf{x}}_j\|^2/\beta)}{\|i-j\|^2} & otherwise \end{cases} \tag{8}$$

The pairwise potential term of CRF models the spatial interaction between neighborhood pixel positions i and j of a hyperspectral image based on their spectral difference. The $\bar{\mathbf{x}}$ represents the selected subset of spectral bands. θ controls the corresponding strength, and β can be set to twice the mean square value of the spectral difference of all adjacent pixels in the hyperspectral image. Based on Eq.(8), the pairwise potential term penalizes the spatial inconsistencies of adjacent pixel classification categories based on the spectral difference, so that the pairwise potential term favors the homogenous regions of a hyperspectral image take the same classification label. Compared to unary potential term, the pairwise potential function considers the spatial patterns to eliminate the uncertainty between spectrum and class mapping by modeling the spatial interaction of neighboring pixels. Therefore, CRF can integrate the spectral and spatial information using the unary and pairwise potentials to alleviate the effects of spectral variability.

III. Experimental data

In our experimental set-up, we apply three hyperspectral datasets from different experimental areas and different sensors to analyze the performance of the CRFBS method. These obtained hyperspectral images have some bands contaminated with severe noise, which are expected to have a certain impact on the classification accuracy. In practice, low-noise spectral bands are often used, and some severely noisy bands are removed in advance, based on expert knowledge. Considering that the proposed algorithm can directly deal with the original hyperspectral image with noisy bands by integrating band selection based on the relative importance of the spectral bands, the obtained raw hyperspectral data with noise spectral bands are used to verify the effectiveness of the CRFBS method.

The first experimental dataset is the publicly available Indian Pines hyperspectral data, which was acquired by the Airborne/Visible Infrared Imaging Spectrometer (AVIRIS) sensor. The hyperspectral image contains 145 × 145 pixels with 20 m spatial resolution and 224 spectral channels between 0.4 and 2.5 μm. However, the data we actually obtain have only 220 spectral channels, and these spectral channels are used directly in our experiments. There are 16 thematic classes in the Indian Pines dataset. The overall appearance of the experimental area and the corresponding category distribution are presented in Fig. 2(a) and (b), respectively. The detailed class information containing the number of training and test samples for the Indian Pines dataset is provided in Table I.

The Salinas hyperspectral dataset used in the second experiment was acquired by the AVIRIS sensor from the Salinas Valley, California. The hyperspectral image has 512 × 217 pixels with 3.7 m spatial resolution. The Salinas dataset originally has 224 spectral bands between 0.4 and 2.5 μm, which contains 20 water absorption spectral bands. All these spectral channels are used in our experiments, and no bands have been discarded in advance. As shown in Fig. 3, an overview and the spatial distribution of 16 agricultural types are given. In this experiment, only 15 labeled pixels for each class were selected as training samples, due to the relatively high separability between most categories of the Salinas dataset. The detailed class information used for classification is reported in Table II.

The third experimental dataset is the WHU-Hi-HanChuan UAV dataset from Hanchuan [47], Hubei province, China, which was acquired by a Headwall Nano-Hyperspec sensor mounted on Aibot X6 six-rotor UAV in June 2016. The acquired hyperspectral image contains 303 × 1217 pixels and 274 spectral channels between 400 and 1000 nm with several severe noise bands. The spatial resolution of the image is 0.1 m, since the flight height of the UAV was set to 250 m. Fig. 4(a) gives an overview of this study area based on obtained visible data and some photos of the typical crop types from field investigation. The image mainly has 16 semantic classes, which were labeled in detail and cover almost the whole of the image to effectively evaluate classification algorithms. The corresponding hyperspectral image and spatial distribution of the various categories are shown in Fig. 4 (b) and Fig. 4 (c). In this experiment, the numbers of training and test samples are given in Table III.

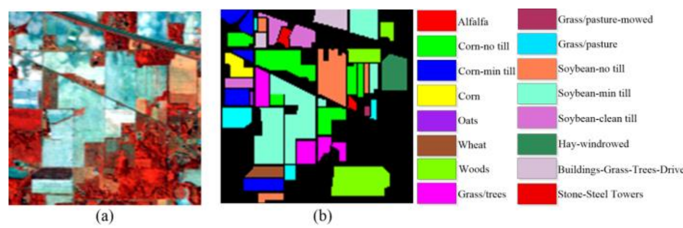

Fig. 2. Indian Pines dataset. (a) Three-band false color image. (b) Ground-truth image.

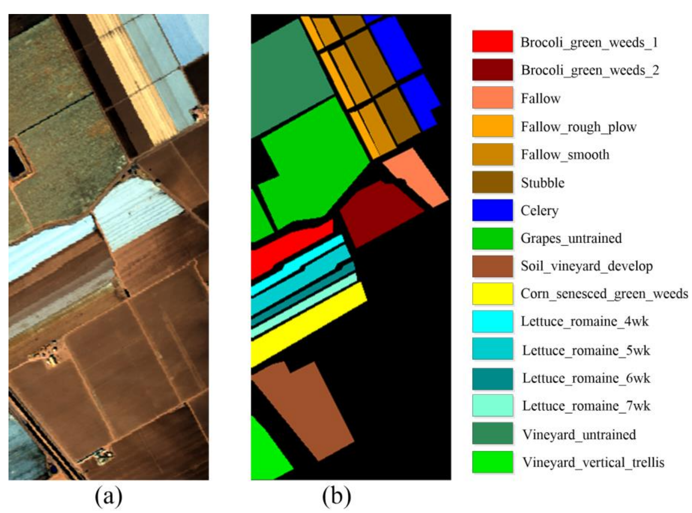

Fig. 3. Salinas dataset. (a) Three-band false color image. (b) Ground-truth image.

This article has been accepted for publication in a future issue of this journal, but has not been fully edited. Content may change prior to final publication. Citation information: DOI 10.1109/JSTARS.2020.2984568, IEEE Journal of Selected Topics in Applied Earth Observations and Remote Sensing

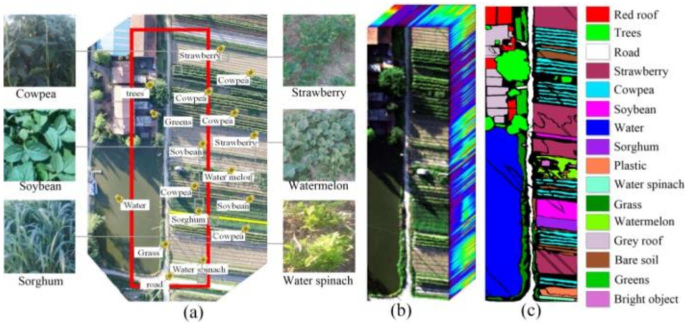

Fig. 4. WHU-Hi-HanChuan UAV dataset. (a) Visible data and photos of the some typical crop types in the study area. (b) Hyperspectral image. (c) Ground-truth image.

TABLE I
CLASS INFORMATION FOR THE INDIAN PINES IMAGE.

No.	Class name	Training samples	Test samples
C1	Alfalfa	23	23
C2	Corn-no till	50	1378
C3	Corn-min till	50	780
C4	Corn	50	187
C5	Grass/pasture	50	433
C6	Grass/trees	50	680
C7	Grass/pasture-mowed	14	14
C8	Hay-windrowed	50	428
C9	Oats	10	10
C10	Soybean-no till	50	922
C11	Soybean-min till	50	2405
C12	Soybean-clean till	50	543
C13	Wheat	50	155
C14	Woods	50	1215
C15	Buildings-Grass-Trees-Drives	50	336
C16	Stone-Steel Towers	47	46

TABLE II
CLASS INFORMATION FOR THE SALINAS IMAGE.

No.	Class name	Training samples	Test samples
C1	Brocoli_green_weeds_1	15	1994
C2	Brocoli_green_weeds_2	15	3711
C3	Fallow	15	1961
C4	Fallow_rough_plow	15	1379
C5	Fallow_smooth	15	2663
C6	Stubble	15	3944
C7	Celery	15	3564
C8	Grapes_untrained	15	11256
C9	Soil_vineyard_develop	15	6188
C10	Corn_senesced_green_weeds	15	3263
C11	Lettuce_romaine_4wk	15	1053
C12	Lettuce_romaine_5wk	15	1912
C13	Lettuce_romaine_6wk	15	901
C14	Lettuce_romaine_7wk	15	1055
C15	Vineyard_untrained	15	7253
C16	Vineyard_vertical_trellis	15	1792

TABLE III
CLASS INFORMATION FOR THE WHU-HI-HANCHUAN UAV IMAGE.

No.	Class name	Training samples	Test samples
C1	Red roof	50	10466
C2	Trees	50	17928
C3	Road	50	18510
C4	Strawberry	50	44685
C5	Cowpea	50	22703
C6	Soybean	50	10237
C7	Water	50	75351
C8	Sorghum	50	5303
C9	Plastic	50	3629
C10	Water spinach	50	1150
C11	Grass	50	9419
C12	Watermelon	50	4483
C13	Gray roof	50	16861
C14	Bare soil	50	9066
C15	Greens	50	5853
C16	Bright object	50	1086

IV. RESULTS AND ANALYSIS

In this section, the experimental results using different hyperspectral datasets are described and analyzed to test the effectiveness of the CRFBS algorithm. CRFBS was compared with several state-of-art classification methods, including pixel-wise, object-oriented and deep learning approaches. For the pixel-wise classification method, SVM was selected as the comparison algorithm, which uses an RBF kernel and is implemented in LIBSVM [46]. For the object-oriented classification method, a multi-resolution segmentation algorithm implemented in eCognition 8.0 (FNEA) was used to obtain segmentation objects, and a majority voting strategy was applied to obtain the object-oriented classification map based on the pixel-wise SVM classification map. The corresponding object-oriented approach is denoted by OO-FNEA in our study. The deep learning approach used as a comparison algorithm was the spectral-spatial attention network (SSAN) [32], which extracts spectral-spatial features based on a spectral attention bi-directional recurrent neural network branch and a spatial attention CNN branch.

In addition, the band selection based on band importance is integrated in the CRFBS algorithm, which is denoted as BIBS in our study, so that the improvement of this mechanism can be evaluated. To verify that band importance can be used for feature selection, the BIBS method is compared with some state-of-art band selection approaches: the band selection method based on saliency bands and scale selection (SBSS) [11] and the supervised band selection based on modified ant lion optimizer (MALO) [48]. All bands of hyperspectral imagery are also used as a benchmark, which is denoted as AllBands. The optimal selected feature subset obtained by these band selection methods (SBSS, MALO, and BIBS) as well as all bands of the hyperspectral imagery are used as input to the SVM to achieve a pixel-wise classification performance.

The classification maps for the various classification methods (AllBands, SBSS, MALO, BIBS, OO-FNEA, SSAN, and CRFBS) with the Indian Pines, Salinas, and WHU-Hi-HanChuan UAV datasets are shown in Figs. 5–7 respectively. They allow for a qualitative assessment of the results. To quantitatively evaluate these classification results, several common measures of classification accuracies are used, including the accuracy of each class, the overall accuracy (OA), the average accuracy (AA), and the Kappa coefficient (KAPPA). The corresponding classification accuracies are reported in Table IV–VI for the Indian Pines, Salinas, and WHU-Hi-HanChuan UAV datasets.

For the pixel-wise classification methods (AllBands, SBSS, MALO, and BIBS), as shown in Figs. 5–7, they all present severe salt-and-pepper classification noise mainly because there is no consideration of spatial information, which can effectively reduce the degree of spectral confusion between different categories. These pixel-wise classification algorithms select the corresponding optimal spectral band subset based on different metrics. In consequence they have different classification performances. As reported in Table IV–VI, the proposed band selection methods (BIBS) using the selected band subsets show – compared with all input bands of

This article has been accepted for publication in a future issue of this journal, but has not been fully edited. Content may change prior to final publication. Citation information: DOI 10.1109/JSTARS.2020.2984568, IEEE Journal of Selected Topics in Applied Earth Observations and Remote Sensing

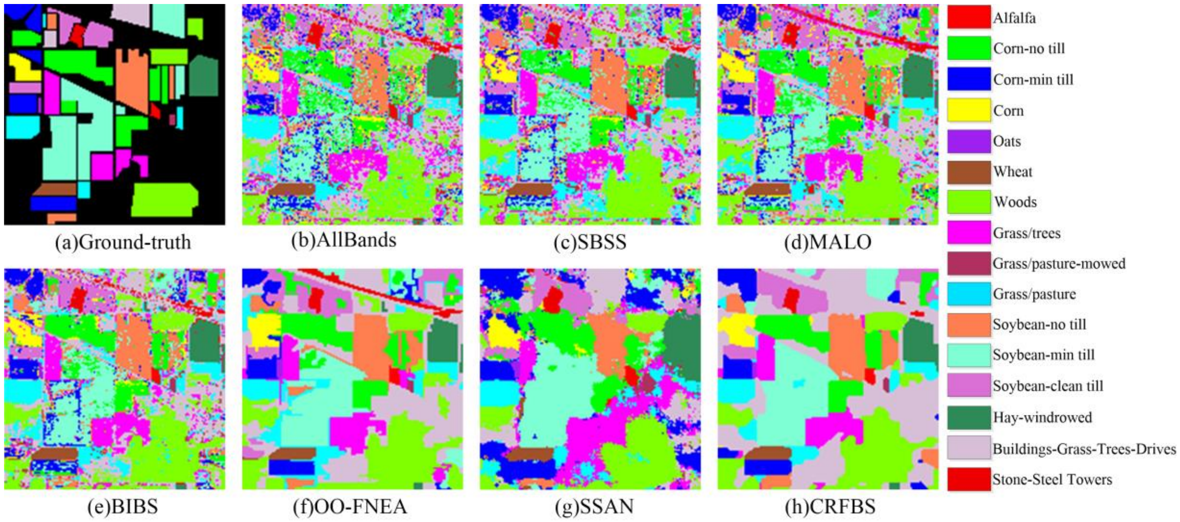

Fig. 5. Classification results for the Indian Pines dataset. (a) Ground-truth (b) AllBands, (c) SBSS, (d) MALO, (e) BIBS, (f) OO-FNEA, (g) SSAN, and (h) CRFBS.

TABLE IV
CLASSIFICATION ACCURACIES FOR THE INDIAN PINES DATASET.

	CLASS	ALLBANDS	SBSS	MALO	BIBS	OO-FNEA	SSAN	CRFBS
Per-category accuracy (%)	Alfalfa	69.57	91.30	95.65	95.65	95.65	**100.00**	95.65
	Corn-no till	56.75	59.07	67.49	73.58	78.01	77.58	**79.54**
	Corn-min till	53.33	62.18	59.74	72.31	82.56	**95.38**	90.38
	Corn	82.35	81.82	91.44	88.77	88.24	90.91	**96.79**
	Grass/pasture	86.14	81.06	91.45	90.99	86.61	91.45	**93.76**
	Grass/trees	87.35	87.06	94.85	95.44	94.56	91.91	**99.12**
	Grass/pasture-mowed	**100.00**	**100.00**	92.86	**100.00**	**100.00**	**100.00**	**100.00**
	Hay-windrowed	96.73	97.66	97.66	98.83	97.66	99.77	**100.00**
	Oats	80.00	70.00	80.00	**100.00**	**100.00**	**100.00**	**100.00**
	Soybean-no till	68.66	81.24	79.07	84.06	89.80	81.67	**93.28**
	Soybean-min till	52.56	62.79	59.46	68.77	76.26	86.28	**91.89**
	Soybean-clean till	69.80	79.56	82.14	88.21	84.90	86.19	**98.16**
	Wheat	96.77	96.77	98.71	**99.35**	98.71	**99.35**	**99.35**
	Woods	80.82	**94.07**	92.67	91.44	89.63	86.91	90.21
	Buildings-Grass-Trees-Drives	71.13	55.06	67.26	72.92	88.99	98.21	**100.00**
	Stone-Steel Towers	95.65	91.30	93.48	97.83	97.83	**100.00**	**100.00**
	OA (%)	67.63	73.95	75.58	80.78	84.51	87.49	**91.79**
	KAPPA	0.6345	0.704	0.7235	0.7818	0.8238	0.8568	**0.9061**
	AA (%)	77.98	80.68	84.00	88.64	90.59	92.85	**95.51**

hyperspectral remote sensing images – improved classification accuracy. This is due to the capability to select more informative spectral channels to eliminate the impact of noise bands.

We find the classification accuracy of the proposed BIBS method has been improved by more than 3% compared with the use of all spectral bands. And we find these improvements for the Indian Pines, Salinas, as well as the WHU-Hi-HanChuan UAV datasets. Compared with other band selection methods (SBSS and MALO), BIBS can achieve comparative classification performance, or partly even higher classification accuracy. These classification results illustrate that the band selection method based on the band importance has the capability to select a subset of spectral bands that are beneficial for classification. With it the negative effects of noise bands are lowered and thus, classification performance is improved.

For the spectral-spatial classification methods, the object-oriented approach and the deep learning algorithm deliver smoother classification results. Beyond they improve classification accuracies by considering spatial contextual information, compared with the pixel-wise approaches. As shown in Figs. 5–7(f), the classification maps of OO-FNEA method tend to be more regular due to the constraints of segmentation results. However, it remains an unsolved challenge to select optimal segmentation scales [22] because of the scale diversity of the different classification types. Thus, some similar categories may be misclassified, such as the vineyard_untrained and the grapes_untrained classes in Fig. 6. The deep learning method (SSAN) exhibits better classification accuracy than OO-FNEA due to the strong learning ability and spatial information utilization ability of deep learning. In the case of limited training samples, the SSAN algorithm still causes confusion in some similar categories, such as corn-no till and soybean-min till categories in Fig. 5.

For the proposed CRFBS algorithm, the band selection based on the relative utility of the spectral bands is integrated to select important bands that are beneficial for classification and to alleviate the effects of input noise spectral bands. On the other hand, the spatial interactions of pixels are considered by pairwise potentials of CRF to provide the complementary

This article has been accepted for publication in a future issue of this journal, but has not been fully edited. Content may change prior to final publication. Citation information: DOI 10.1109/JSTARS.2020.2984568, IEEE Journal of Selected Topics in Applied Earth Observations and Remote Sensing

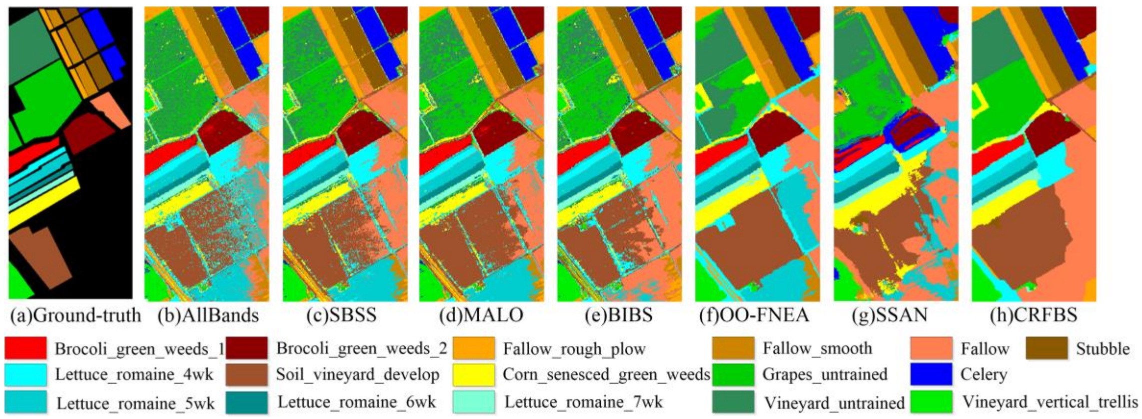

Fig. 6. Classification results for the Salinas dataset. (a) Ground-truth (b) AllBands, (c) SBSS, (d) MALO, (e) BIBS, (f) OO-FNEA, (g) SSAN, and (h) CRFBS.

TABLE V
CLASSIFICATION ACCURACIES FOR THE SALINAS DATASET.

	CLASS	ALLBANDS	SBSS	MALO	BIBS	OO-FNEA	SSAN	CRFBS
Per-category accuracy (%)	Brocoli_green_weeds_1	97.69	96.99	98.14	99.30	99.85	79.94	**100.00**
	Brocoli_green_weeds_2	92.59	96.44	95.93	97.93	**100.00**	58.66	99.68
	Fallow	75.52	95.97	94.75	96.94	**100.00**	90.97	**100.00**
	Fallow_rough_plow	98.19	97.97	98.19	98.84	**100.00**	94.92	**100.00**
	Fallow_smooth	83.55	86.93	92.41	88.32	96.92	**99.92**	98.91
	Stubble	99.67	99.19	99.62	99.75	99.47	99.42	**100.00**
	Celery	99.35	99.47	99.49	99.41	99.13	98.68	**99.86**
	Grapes_untrained	44.00	66.66	67.01	70.57	51.00	74.37	**98.58**
	Soil_vineyard_develop	96.38	97.56	97.66	97.22	**100.00**	94.21	**100.00**
	Corn_senesced_green_weeds	81.67	75.39	73.09	82.01	96.94	**97.79**	92.64
	Lettuce_romaine_4wk	96.11	96.30	96.20	95.92	90.12	96.58	**100.00**
	Lettuce_romaine_5wk	98.59	**100.00**	99.53	99.84	**100.00**	94.67	**100.00**
	Lettuce_romaine_6wk	98.11	96.45	99.11	99.00	97.11	**100.00**	98.22
	Lettuce_romaine_7wk	90.43	93.08	92.61	91.85	89.95	96.97	**98.01**
	Vineyard_untrained	59.62	65.15	65.78	65.71	86.87	85.37	**99.50**
	Vineyard_vertical_trellis	94.87	96.60	95.42	98.33	**100.00**	90.40	**100.00**
	OA (%)	78.41	84.90	85.18	86.57	87.12	87.06	**99.04**
	KAPPA	0.7613	0.8323	0.8353	0.8508	0.8577	0.8566	**0.9893**
	AA (%)	87.90	91.26	91.56	92.56	94.21	90.80	**99.09**

information for spectral cues from the spatial dimension to improve the separability between classification categories. Accordingly, the CRFBS algorithm delivers an improved classification performance in both, the evaluation of the classification maps in a qualitative sense as well as the quantitative results. As reported in Table IV–VI, CRFBS shows better classification accuracies. And it shows an increase of more than 11% in OA over the highest accuracy of the pixel-wise approaches for the Indian Pines, Salinas, and WHU-Hi-HanChuan UAV datasets. Compared with the spectral-spatial classification methods (OO-FNEA and SSAN), CRFBS also leads to better classification accuracies and visual results. For example, CRFBS can correctly distinguish the vineyard_untrained and the grapes_untrained classes in Fig. 6, and shows an improvement for these classes in classification maps and classification accuracies. Overall, we find the spectral-spatial classification methods (OO-FNEA and SSAN) can achieve reasonable classification results, and the CRFBS method exhibits a competitive classification performance for the Indian Pines, Salinas, and WHU-Hi-HanChuan UAV datasets.

V. DISCUSSION

A. *The effect of important bands for classification accuracy of the SVM and RF approaches*

The CRFBS method integrates the band selection based on band importance to select the bands that are useful for classification, and this relative utility level of the spectral channels is obtained by the RF method. The original input hyperspectral image often has noisy spectral bands, so that the classification effect of important bands after removing noise bands for the SVM and RF approaches is analyzed, and the rationality of integrating these methods is explained in this section. Thereby, additional experiments were conducted using SVM and RF classifiers with all spectral bands (AllBands) and selected bands based on band importance (BIBS) for the three datasets. In the experiments, the threshold of cumulative band importance keeping ratio σ is set to 0.7, and the corresponding numbers of selected spectral bands using the BIBS algorithm are 118, 103, and 164 for the Indian Pines, Salinas, and WHU-Hi-HanChuan UAV datasets, respectively. The original input spectral bands and the selected important spectral bands were used to analyze the classification effect of the important bands for the SVM and RF approaches. The classification accuracies are reported in Table VII.

This article has been accepted for publication in a future issue of this journal, but has not been fully edited. Content may change prior to final publication. Citation information: DOI 10.1109/JSTARS.2020.2984568, IEEE Journal of Selected Topics in Applied Earth Observations and Remote Sensing

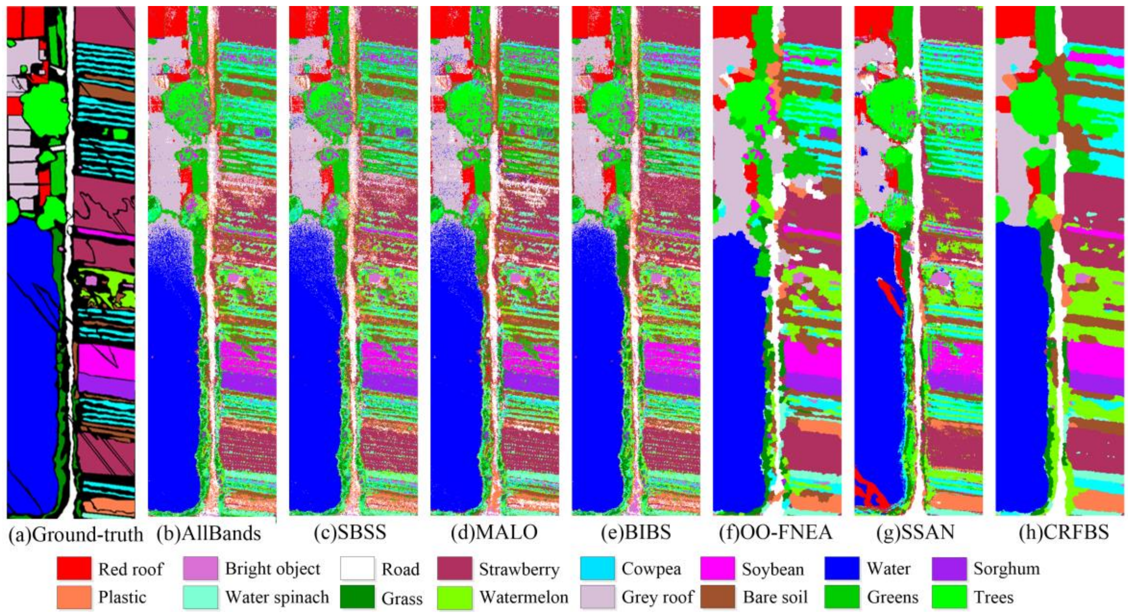

Fig. 7. Classification results for the WHU-Hi-HanChuan UAV dataset. (a) Ground-truth (b) AllBands, (c) SBSS, (d) MALO, (e) BIBS, (f) OO-FNEA, (g) SSAN, and (h) CRFBS.

TABLE VI
CLASSIFICATION ACCURACIES FOR THE WHU-HI-HANCHUAN UAV DATASET.

Class		AllBands	SBSS	MALO	BIBS	OO-FNEA	SSAN	CRFBS
Per-category accuracy (%)	Red roof	82.72	81.25	88.80	86.42	88.30	79.80	**95.24**
	Trees	49.10	42.50	53.34	49.54	59.35	**83.09**	82.41
	Road	63.31	60.71	63.44	60.01	68.84	**91.33**	73.88
	Strawberry	67.71	69.79	66.68	77.77	80.81	83.48	**96.72**
	Cowpea	46.14	38.34	26.55	43.66	59.46	**85.15**	46.55
	Soybean	70.07	71.55	68.95	77.15	92.04	75.69	**97.40**
	Water	90.78	93.35	93.89	95.59	94.34	87.87	**98.14**
	Sorghum	92.61	90.89	90.68	91.27	94.21	88.16	**96.00**
	Plastic	59.52	59.69	53.10	57.10	83.93	95.54	**100.00**
	Water spinach	72.78	71.74	81.65	71.22	98.70	**99.65**	98.17
	Grass	44.42	40.16	32.07	60.46	52.59	56.81	**68.37**
	Watermelon	44.77	43.45	36.81	49.03	72.34	72.36	**95.58**
	Gray roof	95.53	90.95	87.14	92.01	98.80	83.69	**99.19**
	Bare soil	49.11	49.88	49.82	53.97	52.39	64.36	**75.42**
	Greens	87.95	84.95	84.16	78.59	**95.76**	88.55	95.46
	Bright object	69.80	72.65	70.53	74.59	72.47	**88.21**	80.29
OA (%)		72.47	71.70	70.69	75.98	80.99	83.63	**88.31**
KAPPA		0.7251	0.7168	0.7067	0.7589	0.7801	0.8109	**0.8640**
AA (%)		67.89	66.37	65.48	69.90	79.02	82.73	**87.43**

TABLE VII
THE CLASSIFICATION ACCURACIES OF SVM AND RF CLASSIFIERS USING ALL SPECTRAL BANDS (ALLBANDS) AND SELECTED BANDS BASED ON BAND IMPORTANCE (BIBS) FOR THE INDIAN PINES, SALINAS, AND WHU-HI-HANCHUAN UAV DATASETS.

	Indian Pines				Salinas				WHU-Hi-HanChuan UAV			
	SVM		RF		SVM		RF		SVM		RF	
Used bands	AllBands	BIBS	AllBands	BIBS	AllBands	BIBS	AllBands	BIBS	AllBands	BIBS	AllBands	BIBS
OA (%)	67.63	80.78	66.69	69.03	78.41	86.57	80.64	80.60	72.47	75.98	68.71	69.21
KAPPA	0.6345	0.7818	0.6254	0.6512	0.7613	0.8508	0.7859	0.7855	0.7251	0.7589	0.6878	0.6925
AA (%)	77.98	88.64	76.15	78.15	87.90	92.56	89.22	89.08	67.89	69.90	63.07	63.32

From the results shown in Table VII, we draw the conclusion that SVM can achieve a higher classification accuracy when the data are ideal for hyperspectral image classification. SVM shows improvements of more than 6% over RF in OA for the three datasets using the selected important spectral bands. However, the original input hyperspectral image often contains noise bands and uninformative bands, which have a great impact on the SVM algorithm. As reported in Table VII, the SVM algorithm using selected important spectral bands has a higher classification accuracy than that achieved with the original spectral bands. The OA shows a more than 3% improvement for all three experimental data. This demonstrates that it is beneficial to select these important bands to achieve a better classification result. Compared with the SVM approach, we find for the RF algorithm a relatively small impact on classification accuracy using the important bands after removing noise bands. Therefore, to obtain a better classification performance, the advantages of both algorithms are integrated in our research. The RF algorithm is used to select important spectral channels for original input

This article has been accepted for publication in a future issue of this journal, but has not been fully edited. Content may change prior to final publication. Citation information: DOI 10.1109/JSTARS.2020.2984568, IEEE Journal of Selected Topics in Applied Earth Observations and Remote Sensing

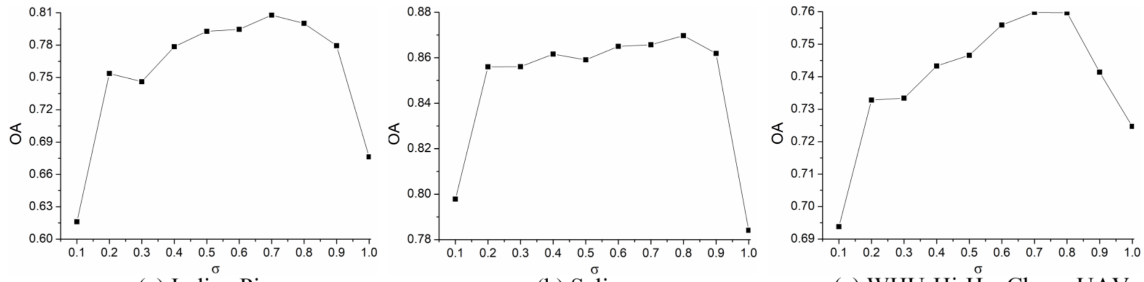

Fig. 8. Sensitivity analysis for threshold of cumulative band importance keeping ratio σ using the Indian Pines, Salinas, and WHU-Hi-HanChuan UAV datasets.

hyperspectral image based on the utility level of the spectral bands. The SVM algorithm uses the selected spectral bands obtained by RF to improve the classification performance in the case of ideal data.

B. Systematic threshold analysis of cumulative band importance keeping ratio for the BIBS algorithm

The threshold of cumulative band importance keeping ratio σ is an important parameter for the band selection based on band importance. This parameter is used to adjust the retention ratio of the cumulative band importance and indirectly affects the number of selected spectral bands. In this subsection, a sensitive analysis of the parameter σ for the BIBS algorithm is given, and additional experiments were conducted to analyze the classification effects using the Indian Pines, Salinas, and WHU-Hi-HanChuan UAV datasets. To analyze the effects of parameter σ, its value was systematically tested from 0.1 to 1, with an interval of 0.1. The corresponding classification accuracies (OA) with different parameter σ are given in Fig. 8.

As shown in Fig. 8, the classification accuracy is at a low level, when the parameter is set to 0.1. This is mainly because only the most important spectral bands are used for classification. Obviously the reduction of spectral bands in this parameter setting is too restrictive, which results in a comparatively low classification accuracy. However, still more the 60% OA is achieved. In the initial stage when the parameter σ increases, classification accuracy increases rapidly since more useful spectral bands for classification are selected. When parameter σ reaches a certain value and most of the information bands have been selected, the classification accuracy can reach the corresponding highest value. After that, when more bands that did not have much effect on classification were added, the classification accuracy showed a decreasing trend. Overall, the threshold of cumulative band importance keeping ratio σ has a great impact on classification accuracy to select the spectral bands with different importance. However, as it can be observed from Fig. 8, we empirically find that there are basically enough important bands used for classification, when the parameter is set to 0.7. The corresponding selected spectral bands are reported in Table VIII for the Indian Pines, Salinas, and WHU-Hi-HanChuan UAV datasets.

As shown in Table VIII, the selected spectral bands have many continuous intervals and the numbers of selected spectral bands are 118, 103, and 164 for the three experimental datasets, respectively. The BIBS only selects the spectral bands that are useful for classification based on band importance measures and adjacent spectral bands always have similar importance due to the correlation between the bands. Accordingly, many spectral bands in continuous intervals with the higher relative utility are selected. In addition, the severe noise bands are less important for classification, and will therefore be explicitly excluded in the selected subset of bands. If we take the Indian Pines dataset as an example, the manually discarded noise bands are 104-108, 150-163, and 220. These bands are also abandoned by the BIBS algorithm due to their lower band importance.

TABLE VIII
THE SELECTED BANDS OF BIBS FOR THE INDIAN PINES, SALINAS, AND WHU-HI-HANCHUAN UAV DATASETS.

Dataset	Selected bands
Indian Pines	2-39, 41, 43-45, 55, 58, 59, 71, 72, 74, 78-86, 92, 93, 95-102, 113-119, 129-136, 139, 141, 142, 167-169, 172-175, 177-187, 189, 194-206, 208
Salinas	5-30, 32-80, 82, 83, 85, 91, 93-96, 101-106, 130-132, 142, 145, 170-173, 175, 182, 190, 216, 217
WHU-Hi-HanChuan UAV	7, 9-32, 34-49, 51-79, 92, 96, 100, 104-108, 113, 116-123, 125-128, 130-146, 154, 158-161, 163-176, 178, 179, 182, 196-201, 203-208, 210-213, 215, 216, 218-221, 223-225, 233, 234, 236, 245, 254, 259, 263, 268, 274

C. The contribution of band selection for the CRFBS algorithm

The band selection based on band importance is used to select spectral channels that are useful for classification and to alleviate the effects of noise bands. On the other hand, the band selection has a great impact on the classification accuracy of the CRFBS algorithm. For evaluation, the contribution of band selection for the CRFBS algorithm is measured in this subsection: we compare the classification results using all spectral bands (AllBands) and selected bands based on band importance (BIBS) for the three experimental datasets (Table IX).

The spectral-spatial classification method based on CRF models the basic discriminative information of various semantic classes based on the used spectral bands by unary potentials. Accordingly, the selected spectral channels also affect the classification results of the CRFBS algorithm. As can be observed from Table IX, the algorithm using the selected bands based on band importance can achieve a more than 3%, 10% and 4% improvement in OA for the Indian Pines, Salinas and WHU-Hi-HanChuan UAV datasets, respectively, compared with that achieved using all spectral bands. This demonstrates that the band selection can improve the spectral-spatial classification accuracies of CRF and play an important role for the CRFBS algorithm.

TABLE IX
THE CLASSIFICATION RESULTS OF CRF USING ALL SPECTRAL BANDS (ALLBANDS) AND SELECTED BANDS BASED ON BAND IMPORTANCE (BIBS) FOR THE INDIAN PINES, SALINAS, AND WHU-HI-HANCHUAN UAV DATASETS.

	Indian Pines		Salinas		WHU-Hi-HanChuan UAV	
	AllBands	BIBS	AllBands	BIBS	AllBands	BIBS
OA (%)	88.10	91.79	82.68	99.04	83.75	88.31
KAPPA	0.8643	0.9061	0.8097	0.9893	0.8121	0.8640
AA (%)	93.72	95.51	92.27	99.09	82.88	87.43

VI. CONCLUSION

In this study, a spectral-spatial classification algorithm based on CRF integrating band selection (CRFBS) has been developed and systematically tested for hyperspectral image with severe noise bands. On the one hand, the hyperspectral data can have very noisy bands, and may even have bands which feature solely zero values and do not contain any useful information. It has been shown that the proposed algorithm can automatically select the bands that are useful for classification to eliminate the effects of severe noise bands and reduce the need for high-quality image data. On the other hand, the CRFBS algorithm can integrate the spectral and spatial information by modeling the spatial interactions between pixels and combining the advantages of the RF and SVM algorithms to improve the classification performance. The experiments using three different hyperspectral datasets with noise bands confirmed that the proposed algorithm can achieve an improvement in classification performance, compared with other state-of-the-art spectral-spatial classification methods. In the future, the accurate estimation of the class membership probabilities will be considered to model the unary potentials of the CRF model, considering the inaccuracy of the probability estimation of the SVM algorithm.

ACKNOWLEDGMENT

The authors would like to thank the editor, associate editor and anonymous reviewers for their helpful comments and suggestions. The authors also would like to thank Mingwei Wang and Xin Hu for their help with the comparison experiments. Ji Zhao gratefully acknowledges the support of K. C. Wong Education Foundation and DAAD.

REFERENCES

[1] C.-I. Chang, *Hyperspectral imaging: techniques for spectral detection and classification*. New York:Kluwer, 2003.
[2] R. Feng, L. Wang, and Y. Zhong, "Least angle regression-based constrained sparse unmixing of hyperspectral remote sensing imagery," *Remote Sensing*, vol. 10, p. 1546, 2018.
[3] L. He, J. Li, C. Liu, and S. Li, "Recent Advances on Spectral–Spatial Hyperspectral Image Classification: An Overview and New Guidelines," *IEEE Trans. Geosci. Remote Sens.*, vol. 56, pp. 1579-1597, 2018.
[4] M. J. Khan, H. S. Khan, A. Yousaf, K. Khurshid, and A. Abbas, "Modern Trends in Hyperspectral Image Analysis: A Review," *IEEE Access*, vol. 6, pp. 14118-14129, 2018.
[5] G. Hughes, "On the mean accuracy of statistical pattern recognizers," *IEEE Trans. Inf. Theory*, vol. 14, pp. 55–63, Jan. 1968.
[6] W. Sun and Q. Du, "Hyperspectral Band Selection: A Review," *IEEE Geosci. Remote Sens. Mag.*, vol. 7, pp. 118-139, 2019.
[7] M. Wang, J. Yu, L. Niu, and W. Sun, "Feature extraction for hyperspectral images using low-rank representation with neighborhood preserving regularization," *IEEE Geosci. Remote Sens. Lett.*, vol. 14, pp. 836-840, 2017.
[8] D. Hong, N. Yokoya, and X. X. Zhu, "Learning a robust local manifold representation for hyperspectral dimensionality reduction," *IEEE J. Sel. Topics Appl. Earth Observ. Remote Sens.*, vol. 10, pp. 2960-2975, 2017.
[9] S. Jia, Z. Ji, Y. Qian, and L. Shen, "Unsupervised band selection for hyperspectral imagery classification without manual band removal," *IEEE J. Sel. Topics Appl. Earth Observ. Remote Sens.*, vol. 5, pp. 531-543, 2012.
[10] W. Sun, L. Tian, Y. Xu, D. Zhang, and Q. Du, "Fast and robust self-representation method for hyperspectral band selection," *IEEE J. Sel. Topics Appl. Earth Observ. Remote Sens.*, vol. 10, pp. 5087-5098, 2017.
[11] P. Su, D. Liu, X. Li, and Z. Liu, "A saliency-based band selection approach for hyperspectral imagery inspired by scale selection," *IEEE Geosci. Remote Sens. Lett.*, vol. 15, pp. 572-576, 2018.
[12] Q. Wang, J. Lin, and Y. Yuan, "Salient band selection for hyperspectral image classification via manifold ranking," *IEEE Trans. Neural Netw. Learn. Syst.*, vol. 27, pp. 1279-1289, 2016.
[13] M. Belgiu and L. Drăguţ, "Random forest in remote sensing: A review of applications and future directions," *ISPRS J. Photogramm. Remote Sens.*, vol. 114, pp. 24-31, Apr. 2016.
[14] G. Mountrakis, J. Im, and C. Ogole, "Support vector machines in remote sensing: A review," *ISPRS J. Photogramm. Remote Sens.*, vol. 66, pp. 247–259, May 2011.
[15] C. Geiß, P. Aravena Pelizari, L. Blickensdörfer, and H. Taubenböck, "Virtual Support Vector Machines with self-learning strategy for classification of multispectral remote sensing imagery," *ISPRS J. Photogramm. Remote Sens.*, vol. 151, pp. 42-58, May 2019.
[16] R. Khatami, G. Mountrakis, and S. V. Stehman, "A meta-analysis of remote sensing research on supervised pixel-based land-cover image classification processes: General guidelines for practitioners and future research," *Remote Sens. Environ.*, vol. 177, pp. 89-100, May 2016.
[17] J. Xia, J. Chanussot, P. Du, and X. He, "Spectral–spatial classification for hyperspectral data using rotation forests with local feature extraction and Markov random fields," *IEEE Trans. Geosci. Remote Sens.*, vol. 53, pp. 2532-2546, 2014.
[18] J. Xia, J. Chanussot, P. Du, and X. He, "Rotation-based support vector machine ensemble in classification of hyperspectral data with limited training samples," *IEEE Trans. Geosci. Remote Sens.*, vol. 54, pp. 1519-1531, 2016.
[19] P. Duan, X. Kang, S. Li, and P. Ghamisi, "Noise-Robust Hyperspectral Image Classification via Multi-Scale Total Variation," *IEEE J. Sel. Topics Appl. Earth Observ. Remote Sens.*, vol. 12, pp. 1948-1962, 2019.
[20] M. Fauvel, Y. Tarabalka, J. A. Benediktsson, J. Chanussot, and J. C. Tilton, "Advances in Spectral–Spatial Classification of Hyperspectral Images," *Proc. IEEE*, vol. 101, pp. 652–675, Mar. 2013.
[21] L. Sun, C. Ma, Y. Chen, H. J. Shim, Z. Wu, and B. Jeon, "Adjacent Superpixel-Based Multiscale Spatial-Spectral Kernel for Hyperspectral Classification," *IEEE J. Sel. Topics Appl. Earth Observ. Remote Sens.*, vol. 12, pp. 1905-1919, 2019.
[22] T. Blaschke, "Object based image analysis for remote sensing," *ISPRS J. Photogramm. Remote Sens.*, vol. 65, pp. 2–16, Jan. 2010.
[23] H. Taubenböck, T. Esch, M. Wurm, A. Roth, and S. Dech, "Object-based feature extraction using high spatial resolution satellite data of urban areas," *Journal of Spatial Science*, vol. 55, pp. 117-132, 2010.
[24] C. Geiß, M. Klotz, A. Schmitt, and H. Taubenböck, "Object-based morphological profiles for classification of remote sensing imagery," *IEEE Trans. Geosci. Remote Sens.*, vol. 54, pp. 5952-5963, 2016.
[25] H. Luo, L. Wang, C. Wu, and L. Zhang, "An improved method for impervious surface mapping incorporating LiDAR data and high-resolution imagery at different acquisition times," *Remote Sensing*, vol. 10, p. 1349, 2018.
[26] M. Baatz and A. Schäpe, "Multiresolution Segmentation: an optimization approach for high quality multi-scale image segmentation," in *Angewandte Geographische Informations-Verarbeitung XII*, Wichmann Verlag, Karlsruhe, 2000, pp. 12–23.
[27] C. Geiß and H. Taubenböck, "Object-based postclassification relearning," *IEEE Geosci. Remote Sens. Lett.*, vol. 12, pp. 2336-2340, 2015.
[28] L. Zhang, L. Zhang, and B. Du, "Deep Learning for Remote Sensing Data: A Technical Tutorial on the State of the Art," *IEEE Geosci. Remote Sens. Mag.*, vol. 4, pp. 22-40, 2016.
[29] N. Audebert, B. Le Saux, and S. Lefevre, "Deep Learning for Classification of Hyperspectral Data," *IEEE Geosci. Remote Sens. Mag.*, vol. 7, pp. 159-173, Jun. 2019.
[30] S. Li, W. Song, L. Fang, Y. Chen, P. Ghamisi, and J. A. Benediktsson, "Deep Learning for Hyperspectral Image Classification: An Overview," *IEEE Trans. Geosci. Remote Sens.*, vol. 57, pp. 6690-6709, Sep. 2019.

This article has been accepted for publication in a future issue of this journal, but has not been fully edited. Content may change prior to final publication. Citation information: DOI 10.1109/JSTARS.2020.2984568, IEEE Journal of Selected Topics in Applied Earth Observations and Remote Sensing

[31] X. Li, Z. Tang, W. Chen, and L. Wang, "Multimodal and Multi-Model Deep Fusion for Fine Classification of Regional Complex Landscape Areas Using ZiYuan-3 Imagery," *Remote Sensing*, vol. 11, p. 2716, 2019.

[32] X. Mei, E. Pan, Y. Ma, X. Dai, J. Huang, F. Fan, Q. Du, H. Zheng, and J. Ma, "Spectral-Spatial Attention Networks for Hyperspectral Image Classification," *Remote Sensing*, vol. 11, p. 963, 2019.

[33] Z. Zhong, J. Li, Z. Luo, and M. Chapman, "Spectral–Spatial Residual Network for Hyperspectral Image Classification: A 3-D Deep Learning Framework," *IEEE Trans. Geosci. Remote Sens.*, vol. 56, pp. 847-858, 2018.

[34] Y. Zhong, J. Zhao, and L. Zhang, "A Hybrid Object-Oriented Conditional Random Field Classification Framework for High Spatial Resolution Remote Sensing Imagery," *IEEE Trans. Geosci. Remote Sens.*, vol. 52, pp. 7023–7037, Nov. 2014.

[35] P. Zhong and R. Wang, "Jointly Learning the Hybrid CRF and MLR Model for Simultaneous Denoising and Classification of Hyperspectral Imagery," *IEEE Trans. Neural Netw. Learn. Syst.*, vol. 25, pp. 1319-1334, Jul. 2014.

[36] J. Zhao, Y. Zhong, and L. Zhang, "Detail-Preserving Smoothing Classifier Based on Conditional Random Fields for High Spatial Resolution Remote Sensing Imagery," *IEEE Trans. Geosci. Remote Sens.*, vol. 53, pp. 2440–2452, May 2015.

[37] J. Li, J. M. Bioucas-Dias, and A. Plaza, "Spectral-Spatial Classification of Hyperspectral Data Using Loopy Belief Propagation and Active Learning," *IEEE Trans. Geosci. Remote Sens.*, vol. 51, pp. 844–856, Feb. 2013.

[38] J. Zhao, Y. Zhong, T. Jia, X. Wang, Y. Xu, H. Shu, and L. Zhang, "Spectral-spatial classification of hyperspectral imagery with cooperative game," *ISPRS J. Photogramm. Remote Sens.*, vol. 135, pp. 31-42, Jan. 2018.

[39] J. D. Lafferty, A. McCallum, and F. C. N. Pereira, "Conditional Random Fields: Probabilistic Models for Segmenting and Labeling Sequence Data," in *Proceedings of the Eighteenth International Conference on Machine Learning*, 2001, pp. 282-289.

[40] J. Zhao, Y. Zhong, H. Shu, and L. Zhang, "High-Resolution Image Classification Integrating Spectral-Spatial-Location Cues by Conditional Random Fields," *IEEE Trans. Image Process.*, vol. 25, pp. 4033–4045, Sept. 2016.

[41] Y. Boykov, O. Veksler, and R. Zabih, "Fast approximate energy minimization via graph cuts," *IEEE Trans. Pattern Anal. Mach. Intell.*, vol. 23, pp. 1222–1239, Nov. 2001.

[42] J. Zhao, Y. Zhong, X. Hu, L. Wei, and L. Zhang, "A robust spectral-spatial approach to identifying heterogeneous crops using remote sensing imagery with high spectral and spatial resolutions," *Remote Sens. Environ.*, vol. 239, p. 111605, Mar. 2020.

[43] L. Breiman, "Random forests," *Machine learning*, vol. 45, pp. 5-32, 2001.

[44] J. Xia, P. Ghamisi, N. Yokoya, and A. Iwasaki, "Random forest ensembles and extended multiextinction profiles for hyperspectral image classification," *IEEE Trans. Geosci. Remote Sens.*, vol. 56, pp. 202-216, 2018.

[45] K. Tan, H. Wang, L. Chen, Q. Du, P. Du, and C. Pan, "Estimation of the spatial distribution of heavy metal in agricultural soils using airborne hyperspectral imaging and random forest," *Journal of hazardous materials*, vol. 382, p. 120987, 2020.

[46] C.-C. Chang and C.-J. Lin, "LIBSVM: a library for support vector machines," *ACM T. Int. Syst. Technol. (TIST)*, vol. 2, pp. 1–27, Apr. 2011.

[47] Y. Zhong, X. Wang, Y. Xu, S. Wang, T. Jia, X. Hu, J. Zhao, L. Wei, and L. Zhang, "Mini-UAV-Borne Hyperspectral Remote Sensing: From Observation and Processing to Applications," *IEEE Geosci. Remote Sens. Mag.*, vol. 6, pp. 46-62, 2018.

[48] M. Wang, C. Wu, L. Wang, D. Xiang, and X. Huang, "A feature selection approach for hyperspectral image based on modified ant lion optimizer," *Knowledge-Based Systems*, vol. 168, pp. 39-48, 2019.

Ji Zhao received the Ph.D. degree in photogrammetry and remote sensing from the State Key Laboratory of Information Engineering in Surveying, Mapping, and Remote Sensing, Wuhan University, China, in 2017. He is now an associate professor at the School of Computer Science, China University of Geosciences, Wuhan.

His major research interests include high resolution remote sensing image classification, scene analysis, remote sensing applications, and machine learning algorithms.

Suzheng Tian received the B.E. degree in computer science and technology from the School of Computer Science, China University of Geosciences, Wuhan, China, in 2019. She is currently pursuing the M.S. degree in the School of Computer Science, China University of Geosciences, Wuhan, China.

Her major research interests include machine learning methods and nighttime lights.

Christian Geiß (M'15) received the M.Sc. degree in applied geoinformatics from the Paris Lodron University of Salzburg, Salzburg, Austria, in 2010, and the Ph.D. degree (Dr. rer. nat.) from the Humboldt University of Berlin, Berlin, Germany, in 2014. Since 2010, he has been with the German Remote Sensing Data Center (DFD), German Aerospace Center (DLR), Weßling, Germany. In 2017, he was also with the Cambridge University Centre for Risk in the Built Environment (CURBE), University of Cambridge, Cambridge, U.K., as a Visiting Scholar.

His current research interests include the development of machine learning methods for the interpretation of earth observation data, multimodal remote sensing of the built environment, exposure and vulnerability assessment in the context of natural hazards, and techniques for automated damage assessment after natural disasters.

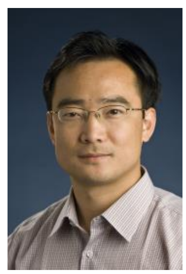

Lizhe Wang is the "ChuTian" Chair Professor at School of Computer Science, China Univ. of Geosciences. He received B.E. & M.E from Tsinghua Univ. and D.E. from Univ. Karlsruhe (Magna Cum Laude), Germany.

His research interests include remote sensing data processing, Digital Earth, Big Data Computing. He is a fellow of IET and BCS and Associate Editor of Remote Sensing, IJDE, etc. He is the recipient of Distinguished Young Scholars of NSFC, National Leading Talents of Science & Technology Innovation, 100-Talents Program of Chinese Academy of Sciences.

Yanfei Zhong (M'11-SM'15) received the B.S. degree in information engineering and the Ph.D. degree in photogrammetry and remote sensing from Wuhan University, China, in 2002 and 2007, respectively.

Since 2010, He has been a Full professor with the State Key Laboratory of Information Engineering in Surveying, Mapping and Remote Sensing (LIESMARS), Wuhan University, China. He organized the Intelligent Data Extraction, Analysis and Applications of Remote Sensing (RSIDEA) research group. He has published more than 100 research papers in international journals, such as *Remote Sensing of Environment*, *ISPRS Journal of Photogrammetry and Remote Sensing*, IEEE TRANSACTIONS ON GEOSCIENCE AND REMOTE SENSING. His research interests include hyperspectral remote sensing information processing, high-resolution remote sensing image understanding, and geoscience interpretation for multisource remote sensing data and applications.

Dr. Zhong is a Fellow of the Institution of Engineering and Technology (IET). He was a recipient of the 2016 Best Paper Theoretical Innovation Award from the International Society for Optics and Photonics (SPIE). He won the Second-Place Prize in 2013 IEEE GRSS Data Fusion Contest and the Single-view Semantic 3-D Challenge of the 2019 IEEE GRSS Data Fusion Contest, respectively. He is currently serving as an Associate Editor for the

IEEE JOURNAL OF SELECTED TOPICS IN APPLIED EARTH OBSERVATIONS AND REMOTE SENSING, and the *International Journal of Remote Sensing*.

Hannes Taubenböck received the Diploma in geography from the Ludwig-Maximilians-Universität München, Munich, Germany, in 2004, and the Ph.D. degree (Dr. rer. nat.) in geography from the JuliusMaximilians-Universität Würzburg, Würzburg, Germany, in 2008.

In 2005, he joined the German Remote Sensing Data Center (DFD), German Aerospace Center (DLR), Oberpfaffenhofen, Germany. After a postdoctoral research phase with the University of Würzburg (2007–2010), he returned in 2010 to DLR–DFD as a scientific employee. In 2013, he became the Head of the “City and Society” team. In 2019, he habilitated at the University of Würzburg in geography. His current research focuses on urban remote sensing topics, from the development of algorithms for information extraction to value adding to classification products for findings in urban geography.